

STRUCTURAL AND DYNAMICAL UNCERTAINTIES IN MODELING AXISYMMETRIC ELLIPTICAL GALAXIES

Aaron J. Romanowsky

Christopher S. Kochanek

Harvard-Smithsonian Center for Astrophysics, MS-10,
60 Garden Street, Cambridge MA 02138
Email: aromanowsky@cfa.harvard.edu

ABSTRACT

Quantitative dynamical models of galaxies require deprojecting the observed surface brightness to determine the luminosity density of the galaxy. Existing deprojection methods for axisymmetric galaxies assume that a unique deprojection exists for any given inclination, even though the projected density is known to be degenerate to the addition of “konus densities” that are invisible in projection. We develop a deprojection method based on linear regularization that can explore the range of luminosity densities statistically consistent with an observed surface brightness distribution. The luminosity density is poorly constrained at modest inclinations ($i \gtrsim 30^\circ$), even in the limit of vanishing observational errors. In constant mass-to-light ratio, axisymmetric, two-integral dynamical models, the uncertainties in the luminosity density result in large uncertainties in the meridional plane velocities. However, the projected line-of-sight velocities show variations comparable to current typical observational uncertainties.

Subject headings: galaxies: elliptical and lenticular, cD — galaxies: individual (NGC 1439, NGC 7619) — galaxies: kinematics and dynamics — galaxies: structure

1. INTRODUCTION

Models of elliptical galaxies seek to understand the spatial distribution of their stars (e.g. Franx, Illingworth, & de Zeeuw 1991; Statler 1995), the structure of their orbits (Dehnen & Gerhard 1993, 1994; Arnold, Robijn, & de Zeeuw 1995), and to secure evidence for the presence of dark halos (Saglia et al. 1993; Carollo et al. 1995) or black holes (van der Marel et al. 1994; Dehnen 1995). These problems can be probed using the observed velocities of the stars (van der Marel 1991; Carollo & Danziger 1994), X-ray emission (Fabbiano 1989, 1995), gaseous disks and rings (Schweizer, Whitmore, & Rubin 1983; Whitmore, McElroy, & Schweizer 1987; Bertola et al. 1991; Franx, van Gorkom, & de Zeeuw 1994), and gravitational lenses (Maoz & Rix 1993; Kochanek 1995, 1996). Most modern dynamical models employ axisymmetric, two-integral models in which the distribution function depends only on the energy and the angular momentum about the symmetry

axis (e.g. Binney, Davies, & Illingworth 1990; Hunter & Qian 1993). Such models have simple solutions to the Jeans equations (Satoh 1980; see also Binney & Tremaine 1987 §4.2), and in some cases the distribution function can be determined (Dehnen & Gerhard 1993, 1994; Qian et al. 1995). Quantitative application of the two-integral models to a real galaxy relies on the deprojection of the observed surface brightness of the galaxy to determine its three-dimensional luminosity density.

The uniqueness of the deprojection of a galaxy depends on the symmetries of the density. Spherical galaxies always have unique deprojections, and ellipsoidal galaxies with fixed axes have unique deprojections for known inclinations (e.g. Binney 1985). General axisymmetric galaxies do not have unique deprojections, except when the symmetry axis is in the plane of the sky (inclination $i = 90^\circ$, Rybicki 1987). The projection operation destroys information about the Fourier components of the density which lie in a “cone of ignorance” of opening angle $90^\circ - i$ about the symmetry axis. A “konus density” (Gerhard & Binney 1996), whose Fourier transform is non-zero only inside the cone of ignorance, can be added to the luminosity density without changing the projected surface brightness. Kochanek & Rybicki (1996) developed methods to produce families of konus densities with arbitrary equatorial density distributions. Simple konus densities generally look like “disks” because of the conical symmetry of the model in Fourier space; this is consistent with Rix & White’s (1990) observation that disks would be nearly invisible in ellipticals, unless close to edge-on.

We need to explore two issues to understand the effects of the deprojection degeneracy on axisymmetric models of ellipticals. The first issue is the existence of smooth konus densities. A real galaxy must have a smooth, monotonic, positive definite density profile. These physical restrictions limit the allowed range of konus densities. For example, none of the analytic konus densities of Gerhard & Binney (1996) or Kochanek & Rybicki (1996) are physical because they have unacceptable angular profiles at large radii due to the conditions imposed to find analytic solutions. The second issue is that even if the luminosity density is underconstrained, the degeneracy is dynamically interesting only if the inferred velocity dispersions or velocity dispersion profiles are uncertain by more than the observational errors.

The projection operator \mathbf{P} is a linear operator $I = \mathbf{P}\nu$ between the luminosity density ν and the surface brightness I . Deprojection corresponds to inverting the linear operator $\nu = \mathbf{P}^{-1}I$. Methods to invert \mathbf{P} must cope with three generic problems: true degeneracies, limited sampling, and amplification of noise. True degeneracies, such as the konus densities, correspond to eigenvalues of \mathbf{P} that are zero, and they can be handled only by adding additional constraints on the inversion such as smoothness, positivity, or monotonicity. The surface brightness is always discretely sampled, but we want to determine the continuous luminosity density. If we try to determine the luminosity density at more points than are sampled in the surface brightness, the luminosity density is underconstrained by the data and additional constraints are required to perform the inversion. Most inversions are also ill-conditioned, because some of the eigenvalues of \mathbf{P} are nearly zero. Small eigenvalues of \mathbf{P} are large eigenvalues of \mathbf{P}^{-1} , and they amplify small fluctuations of I into large fluctuations in ν . The inversion method must suppress these oscillations.

Previous approaches to deprojection produce “unique” inversions because they have additional, hidden constraints. Lucy’s (1974) method is the standard deprojection algorithm used in stellar dynamical models (e.g. Newton & Binney 1987; Binney et al. 1990; van der Marel, Binney, & Davies 1990; Gerhard 1991; van der Marel 1991; Dehnen 1995). It is a simple, iterative scheme that converges toward a density distribution that exactly fits the data; a “unique” solution results because of an implicit, nonparametric bias. Lucy’s method also introduces numerical instabilities into the solution, so the iterations are manually halted at some point when the density still “looks good”. Bendinelli’s (1991) method expands the surface brightness in terms of Gaussian profiles, and then numerically fits the density to these terms. Palmer’s (1994) method finds a finite angular polynomial series for the density whose projection fits the observed surface brightness to arbitrary accuracy. Functional fitting methods are fast, and frequently easy to program, but they are limited to a subset of the possible solutions.

None of these existing methods provides a way of studying the true degeneracies of deprojection and their effects on dynamical models of axisymmetric galaxies. In §2, we develop a deprojection method based on linear regularization that allows us to explore the degeneracies of the inversion while keeping the density well-defined and physical. In §3, we test the algorithm on artificial galaxy images. In §4, we give results for two galaxies (NGC 1439 and NGC 7619), and in §5 we summarize our conclusions. Two appendices add some details of the numerical algorithms.

2. METHODS

2.1. Projection Geometry and Algorithm

An axisymmetric galaxy has density distribution $\nu(X, Y, Z)$, where the Z -axis is the symmetry axis of the galaxy. The surface brightness is $I(x, y)$, where (x, y) are the coordinates in the plane of the sky, and the z -axis lies along the line of sight. The X - and x -axes coincide, and correspond to the line of nodes at the intersection of the plane of the sky and the equatorial plane of the galaxy (thus, for an oblate axisymmetric galaxy, the x -axis corresponds to the observed major axis of the galaxy). Because the galaxy is axisymmetric, its density distribution is completely specified by $\nu(R, Z)$, where $R = \sqrt{X^2 + Y^2}$. For simplicity, we assume that the galaxy has a reflection symmetry about the equatorial plane, $\nu(Z) = \nu(-Z)$. The surface density is related to the luminosity density by the projection operation,

$$I(x, y) = \int_{-\infty}^{+\infty} \nu(R, Z) dz. \quad (1)$$

The transformation between the galaxy’s coordinates and the observer’s coordinates is

$$\begin{aligned} X &= x \\ Y &= y \cos i - z \sin i \\ Z &= y \sin i + z \cos i \\ r^2 = R^2 + Z^2 &= \varpi^2 + z^2, \end{aligned} \quad (2)$$

where $\varpi^2 \equiv x^2 + y^2$, and the inclination $i = 90^\circ$ corresponds to an “edge-on” galaxy with no cone of ignorance.

The density of the galaxy $\nu(R, Z)$ is divided into zones, $\nu_{jk} \equiv \nu(\theta_j, r_k)$, where one quadrant of the meridional plane (R, Z) is divided into N_r radial zones and into N_a angular zones. The radial zones are logarithmically spaced in r from inside ϖ_{\min} to outside ϖ_{\max} , where ϖ_{\min} and ϖ_{\max} are the radii of the inner and outer surface density measurements. The angle θ is the standard spherical polar angle with $\theta = 0$ on the symmetry axis; the angular zones are equally spaced in θ ($\theta_j = j \cdot \Delta\theta$, where $j = [0 \dots N_a - 1]$ and $\Delta\theta = \pi/2N_a$). Reflection symmetry about the equatorial plane is implicit in the model, although the symmetry could be trivially removed.

Although the zones ν_{jk} represent the real density, the projection algorithm considers the galaxy to be made of “stacked blocks” in order to force the density to vary monotonically in angle¹. For an oblate galaxy, the total density of each successive zone increases with its angle θ_j , and each additional contribution can be thought of as a block of density $\check{\nu}_{jk} = p_{jk}^2$ stacked on top of the previous blocks, with total density

$$\nu_{jk} = \sum_{i=0}^{i=j} \check{\nu}_{ik} = \sum_{i=0}^{i=j} p_{ik}^2. \quad (3)$$

By construction, a density model expressed in terms of p_{jk} is positive definite, oblate², and monotonic in angle.

The projected intensity is sampled at discrete points $I_{lm} = I(x_{lm}, y_{lm})$, where l, m are arbitrary indices (e.g. corresponding to polar coordinates ϖ_l, ψ_m). The contribution to I_{lm} from density block $\check{\nu}_{jk}$ is found by integrating along the line of sight through the block

$$dI_{jklm} = \int_{z_1}^{z_2} \check{\nu}_{jk}(z) dz, \quad (4)$$

where (z_1, r_1) , (z_2, r_2) are the coordinates of the intersection points of the line of sight from (x_{lm}, y_{lm}) with the edges of zone $\{jk\}$, and

$$I_{lm} = \sum_{jk} dI_{jklm}. \quad (5)$$

We use a first-order projection scheme that linearly interpolates the density between radially-adjacent zones with

$$\check{\nu}_{jk}(z) = \check{\nu}_{jk} + \frac{\check{\nu}_{jk+1} - \check{\nu}_{jk}}{r_k - r_{k+1}} [r_k - r(z)], \quad (6)$$

¹A general two-dimensional density distribution that is monotonic in both angle and radius cannot be constructed in this way.

²For a prolate galaxy, the density decreases with angle θ_j : $\nu_{jk} = \sum_{i=j}^{N_a-1} \check{\nu}_{ik}$.

giving the first-order approximation

$$dI_{jklm} = \frac{z_2 - z_1}{r_{k+1} - r_k} (\check{\nu}_{jk} r_{k+1} - \check{\nu}_{jk+1} r_k) + \frac{1}{2} \frac{\check{\nu}_{jk+1} - \check{\nu}_{jk}}{r_{k+1} - r_k} \left[z_2 r_2 - z_1 r_1 + \varpi^2 \ln \left(\frac{z_2 + r_2}{z_1 + r_1} \right) \right]_{jklm}. \quad (7)$$

(see Appendix A). Beyond the outermost density zones, the density is assumed to decrease as a power law, normalized to the density of the outermost zone at a given angle θ_j : $\nu \propto \nu_{j0} (r^2 + s_b^2)^{-\alpha_b/2}$. The (small) contribution to the projection from this density “tail” is found by numerical integration of equation (4).

2.2. Smoothing and Regularization

Given the projection, I_{lm} , of the current model density distribution, and the observed surface brightness, I_{lm}^* , we define a χ^2 statistic for the goodness of fit,

$$\chi^2 = \sum_{lm} \left(\frac{I_{lm} - I_{lm}^*}{\sigma_{lm}} \right)^2, \quad (8)$$

where σ_{lm} is the noise associated with the measurement I_{lm}^* (we neglect any correlation function of the noise). If there are N_{data} points I_{lm} , then a good fit should have $\chi^2 \simeq N_{\text{data}}$ with a one standard deviation error of $\Delta\chi^2 \equiv \chi^2 - N_{\text{data}} \simeq \pm\sqrt{2N_{\text{data}}}$ (for $N_{\text{data}} \gg 1$) if we neglect the number of degrees of freedom in the source model. The algorithm used to minimize the function requires the first and second derivatives of the χ^2 with respect to the density kernels p_{lm} ; these derivatives are given in Appendix B.

Linear regularization is used to combat the problems that occur in unregularized solutions of integral equations such as equation (1). The primary problem is the tendency for the density to oscillate between the radial sampling points when there are more model density points than surface sampling points. The simplest solution is to find a good fit to the data while simultaneously minimizing a smoothing function

$$H_1 = \sum_{jk} \left(\frac{h_{jk+1} \nu_{jk+1} - h_{jk} \nu_{jk}}{h_{jk} \nu_{jk}} \right)^2, \quad (9)$$

defined by the fractional variation in the radial density profile, weighted by the bias function $h_{jk} \equiv h(r_k, \theta_j)$. The bias function is used to weight the smoothness equally over all points, and to provide a bias slope at large radii where sky-level uncertainties poorly constrain the radial profile. The density should also vary smoothly with angle, so we add a second smoothing function

$$H_2 = \sum_{jk} \left(\frac{h_{j+1k} \nu_{j+1k} - h_{jk} \nu_{jk}}{h_{jk} \nu_{jk}} \right)^2. \quad (10)$$

to prevent unrealistically sharp angular density variations. Ideally, $h(r, \theta)$ would be given self-consistently by the deprojected radial profile $\nu^{-1}(r, \theta)$. In practice, we fit a simple analytic model,

e.g. the power-law model

$$I(\varpi) = I_0(s_b^2 + \varpi^2)^{(1-\alpha_b)/2}, \quad (11)$$

to the surface data points along the major axis, and analytically deproject it to give $h(r)$; then we assume an constant axis ratio $q_b \equiv b/a$ to give the angular variation $h(r_k, \theta_j)$, e.g.,

$$h_{jk} = \left[s^2 + r_k^2 (\sin^2 \theta_j + \frac{1}{q_b^2} \cos^2 \theta_j) \right]^{\frac{\alpha}{2}}. \quad (12)$$

Such radial surface brightness models qualitatively cover much of the observed range of galactic morphologies (Binney & Tremaine 1987). In addition to enforcing smoothness, the function $h(r, \theta)$ allows us to explicitly bias the profile to some arbitrary morphology.

We then minimize the function $F = \chi^2 + \lambda H$, where $H = H_1 + \kappa H_2$. The weighting factor κ is somewhat arbitrary, but must be small enough to keep the radial profile acceptably smooth. For each image I^* and bias function h , κ is set by trial-and-error to be as large as is possible before significant radial fluctuations appear in the solution. The Lagrange multiplier λ must be adjusted so that when F is minimized, the χ^2 is found to have a value in the range $N_{\text{data}} \pm \sqrt{2N_{\text{data}}}$, where N_{data} is the number of surface density sampling points (we used solutions with χ^2 in the range $N_{\text{data}} \pm \sqrt{N_{\text{data}}}$). The Lagrangian multiplier λ is found iteratively: an initial λ is chosen, the function is minimized, and the resulting χ^2 value is linearly interpolated to $\chi^2 = N_{\text{data}}$ to predict the correct λ ; then the function is again minimized with the new λ , and so on, until the value of the χ^2 falls within the proper range. The minimization is performed using the Polak-Ribiere conjugate gradient method (Press et al. 1992). The expressions for the gradients of χ^2 , H_1 , and H_2 are given in Appendix B.

2.3. Velocity Calculations

To examine the dynamical effects of the projection degeneracies we assume a constant mass-to-light ratio, axisymmetric, two-integral dynamical model (e.g. Binney & Tremaine 1987, van der Marel 1991). Following Binney et al. (1990), we calculate the potential Φ from the mass density $\rho = \Upsilon_0 \nu$ by first expanding the density in Legendre polynomials,

$$\rho_l(r') = \Upsilon_0 \int_0^\pi \nu(r', \theta) P_l(\cos \theta) \sin \theta d\theta \quad (13)$$

and then by finding the potential produced by the Legendre expansion of the density

$$\Phi(r, \theta) = -2\pi G \sum_l P_l(\cos \theta) \left[\frac{1}{r^{(l+1)}} \int_0^r \rho_l(r') r'^{(l+2)} dr' + r^l \int_r^\infty \rho_l(r') \frac{dr'}{r'^{(l-1)}} \right]. \quad (14)$$

The solutions to the Jeans equations for the two-integral model are

$$\nu \sigma^2(R, Z) = \int_Z^\infty \nu(R, Z') \frac{\partial \Phi(R, Z')}{\partial Z'} dZ', \quad (15)$$

and

$$\langle v_\phi^2 \rangle(R, Z) = \sigma^2 + R \frac{\partial \Phi}{\partial R} + \frac{R}{\nu} \frac{\partial(\nu \sigma^2)}{\partial R}, \quad (16)$$

where the galaxy is assumed axisymmetric, steady-state ($\langle v_Z \rangle = \langle v_R \rangle = 0$), and isotropic in the meridional direction ($\sigma_R = \sigma_Z \equiv \sigma$) (see Binney & Tremaine 1987 §4.2). The projected line-of-sight velocity dispersion is

$$I \langle v_{\text{los}}^2 \rangle(x, y) = \int_{-\infty}^{\infty} dz \left[\nu \sigma^2(R, Z) (\cos^2 i + \sin^2 \phi \sin^2 i) + \nu \langle v_\phi^2 \rangle \cos^2 \phi \sin^2 i \right]. \quad (17)$$

$$= \int_{-\infty}^{\infty} \nu \sigma^2(R, Z) dz + \sin^2 i \int_{-\infty}^{\infty} R \cos^2 \phi \left[\nu \frac{\partial \Phi}{\partial R} + \frac{\partial(\nu \sigma^2)}{\partial R} \right] dz. \quad (18)$$

We numerically integrate equations (15) and (16) to find the velocity components σ^2 and $\langle v_\phi^2 \rangle$ in the galaxy's meridional plane, and then we numerically integrate equation (17) to find $\langle v_{\text{los}}^2 \rangle$ (we do not separate out its components $\langle v_{\text{los}}^2 \rangle = \sigma_{\text{los}}^2 + \langle v_{\text{los}} \rangle^2$). The accuracy of the numerical integration algorithm was verified with the analytic solution of Satoh (1980; eqs. [8] and [13]) and other more *ad hoc* analytic solutions.

3. TEST PROBLEMS

We test the method in four stages. First we confirm that if we bias the solution toward the true density, the method converges to the correct result. Next we demonstrate that the deprojection is degenerate by examining the range of solutions we can produce by altering the bias function. To show that the degeneracy is not a numerical artifact, we next investigate the effects of the numerical resolution, observational errors, and numerical errors. Finally we examine the dynamical effects of the degeneracy on the two-integral models.

3.1. Deprojection with Correct Bias

Before examining real galaxies, we studied the deprojection algorithm and the effects of degeneracy with artificial images of known density distributions. We used the axisymmetric, oblate ($q_0 < 1$) density distribution,

$$\nu(R, Z) = \nu_0 \left(1 + \frac{R^2}{s_0^2} + \frac{Z^2}{s_0^2} \frac{1}{q_0^2} \right)^{-\alpha_0/2}, \quad (19)$$

which has the analytically calculable surface brightness,

$$I(x, y) = \frac{\pi^{1/2} \Gamma(\frac{\alpha_0-1}{2})}{\Gamma(\frac{\alpha_0}{2})} \frac{\nu_0 q_0 s_0}{\sqrt{q_0^2 \sin^2 i + \cos^2 i}} \left(1 + \frac{x^2}{s_0^2} + \frac{y^2}{s_0^2} \frac{1}{q_0^2 \sin^2 i + \cos^2 i} \right)^{(1-\alpha_0)/2}. \quad (20)$$

In the test image, the surface brightness points $I_{lm} \equiv I(\varpi_l, \psi_m)$ are logarithmically-spaced in radius ϖ (46 points from $\varpi/s_0 = 0.53$ to $\varpi/s_0 = 38.2$), and equally-spaced in angle ψ (7 points from $\psi = 0$ to $\psi = \pi/2$).

The errors and uncertainties in the image of a bright galaxy are dominated by systematic effects rather than by photon counting noise. Imperfect flat-fielding produces a fractional error which varies over large scales in an image, and the sky background level is uncertain to within some constant value. For a set of image points I_{lm}^* , we adopted an error model with $\sigma_{lm} = \sigma_0 I_{lm}^* + I_b$. To simulate a real image, we added artificial errors to our “data”. A constant background offset, I_b , simulated an error in determining the sky background level, and a Gaussian distribution of fractional errors (with rms amplitude σ_0 , and Fourier width corresponding to fluctuation wavelengths of about 5% the full-frame width of the image) was added to simulate flat-fielding errors. These model errors qualitatively resemble the residuals from fitting real images.

We deprojected simulated images for various values of the model parameters (α_0, s_0, q_0, i), the biasing parameters (α_b, s_b, q_b), and error levels (σ_0, I_b). The results of some of these deprojections are shown in Figure 1, where the image has the analytic form specified by equation (20), with $\alpha_0 = 3.0$, $s_0 = 1.7$, $q_0 = 0.6$, $\sigma_0 = 0.01$ (corresponding to a 0.01 magnitude error), $I_b \simeq 0.0004 I_{\max}^*$ (sky level underestimated), and $i = 30^\circ$ (recall that $i = 0^\circ$ is pole-on), with simulated errors added as described above. The first column of Figure 1 shows the case in which we set the bias function equal to the “correct” density: $h = \nu_{\text{corr}}^{-1}$ (i.e., $\alpha_b = \alpha_0$, $s_b = s_0$, $q_b = q_0$). In this test case, the final solution almost exactly matches the input model, with rms fractional errors of: $\langle(\nu - \nu_{\text{corr}})/\nu_{\text{corr}}\rangle_{\text{rms}} = 0.009$. Similar deprojections were performed over a wide range of model parameters, with similar results: when given the proper bias functions, the algorithm reconstructed the original density function. Large changes in the artificial error parameters had negligible effects.

3.2. The Existence of Degeneracies

Our real interest, however, is how the results can differ from the input density model given the degeneracies in the projection operator. Figure 1 also shows three other deprojections of the same image, where each column shows a solution with a different bias function h . We deliberately chose extreme biases and a low inclination ($i = 30^\circ$) to highlight the range of possible solutions. In the second column, the bias function is more elliptical than the “correct” solution ($\alpha_b = 3.0$, $s_b = 1.7$, $q_b = 0.3$); in the third column it decreases more rapidly with radius ($\alpha_b = 3.5$, $s_b = 2.0$, $q_b = 0.6$); and in the fourth column we have added an exponential disk ($h^{-1} = \nu_{\text{corr}} + k_d \exp(-R/R_b) \text{sech}(Z/Z_b)$, with $k_d = 0.25$, $R_b/s_0 = 5.2$, and $Z_b/s_0 = 0.9$). Each model is converged until it is a statistically acceptable fit to the data ($\chi^2 \simeq N_{\text{data}}$). The rms fractional differences in the density for the solutions are $\langle(\nu - \nu_{\text{corr}})/\nu_{\text{corr}}\rangle_{\text{rms}} = 0.58$, 0.35, and 0.22, for columns 2, 3, and 4, respectively, demonstrating that the konus densities can have large amplitudes. These densities qualitatively resemble the disks examined by Rix & White (1990) and the analytic solutions of Gerhard & Binney (1996) and Kochanek & Rybicki (1996), without the

discontinuity problems exhibited by those solutions at large radii. Although some of the solutions show systematic deviations in the outer regions of the galaxy at the two-sigma level, and the density structure of the disk-biased solution has some unphysical features, it should be remembered that we deliberately chose the bias functions to find extreme examples.

3.3. Searching for “True” Konus Densities

We next checked the effects on the solutions of varying the numerical resolution. A true projection degeneracy should exist independently of the sampling of either the image or the density distribution, except in the limit that the data overconstraints the density. Our standard $N_r \times N_a$ density grid has $N_r = 100$ radial and $N_a = 25$ angular zones. There are numerical errors in the projection, and if we compute the errors for the test problem in §3.1, the contributions to χ^2/N_{data} from numerical errors are $\simeq 0.003$, 0.01 , and 0.07 for $i = 30^\circ$, 60° , and 90° respectively, given our standard error model. Although these numerical errors are much smaller than the observational errors ($\chi^2/N_{\text{data}} \simeq 1$), we must examine whether the magnitude of the degeneracies is influenced by the resolution.

We performed a series of tests comparing the numerical projection of the test model to the analytic projection of the test model, gradually reducing the density zone resolution. Reduced resolution increases the numerical projection errors and reduces the range of possible solutions because the number of degrees of freedom in the density model ($N_r \times N_a$) approaches the number of data points ($N_{\text{data}} = 322$). The inclination was fixed at $i = 30^\circ$. For zone resolutions of $N_r \times N_a = 2500$, 1600 , 400 , 196 , and 100 , the resulting numerical errors were $\chi^2_{\text{err}}/N_{\text{data}} \simeq 0.003$, 0.008 , 0.2 , 1.2 , and 6.0 , respectively. The χ^2 from numerical errors became unacceptable only in the two lowest resolution simulations, where the density distribution was overconstrained ($N_{\text{zones}} \equiv N_r \times N_a < N_{\text{data}}$).

Next we deprojected the test model ($q_0 = 0.6$) using substantially rounder ($q_b = 0.9$) or flatter ($q_b = 0.3$) bias densities. As we reduced the resolution, the allowed degeneracy towards low-ellipticity models was little affected, but the degeneracy towards high-ellipticity models was substantially reduced (see Figure 2). The amplitude of the degeneracy did not change between our standard resolution and the next lowest resolution. The inability to produce high ellipticity models at low numerical resolutions is due to the decreasing angular resolution. Note, however, that the degeneracies still exist even when the data overconstraints the density, a clear sign that the degeneracies are not due to the numerical resolution of the calculation.

A true degeneracy should also exist independently of the observational errors. The amplitude of the degeneracy may increase with the amount of noise in the observations, but it should not vanish in the limit of no noise. We made a sequence of deprojections of a single image while gradually reducing the observational error levels, σ_0 and I_b , until the numerical errors become significant ($\chi^2_{\text{err}}/N_{\text{data}} \sim 0.1$); I_b was reduced in proportion to σ_0 . Figure 3 shows the deprojections

of the same image used in Figure 1 ($\alpha_0 = 3.0, s_0 = 1.7, q_0 = 0.6$), biased to either $q_b = 0.9$ and $q_b = 0.3$ as a function of the inclination ($90^\circ, 60^\circ$, or 30°), with varying errors. The permitted range of the solutions depends strongly on the inclination and weakly on the errors. At $i = 90^\circ$ the solution is unique, with any uncertainty in the axis ratio due to the noise; the rms fractional density variation between the extreme solutions ($q_b = 0.9, 0.3$) at “normal” noise levels ($\sigma_0 = 0.01$) is $\langle(\nu_{0.3} - \nu_{0.9})/\nu_{0.9}\rangle_{\text{rms}} = 0.26$. At $i = 60^\circ$ the axis ratio can be biased upwards and downwards by $\Delta q \sim 0.1$ about the true axis ratio; for $\sigma_0 = 0.01$, the allowed rms variation is $\langle(\nu_{0.3} - \nu_{0.9})/\nu_{0.9}\rangle_{\text{rms}} = 0.53$. At $i = 30^\circ$ the axis ratio can be biased by $\Delta q \sim 0.2$ about the true axis ratio. For $\sigma_0 = 0.01$, the allowed rms variation is $\langle(\nu_{0.3} - \nu_{0.9})/\nu_{0.9}\rangle_{\text{rms}} = 0.82$; even when the errors are at the level of 0.002 magnitudes, the allowed rms variation is $\langle(\nu_{0.3} - \nu_{0.9})/\nu_{0.9}\rangle_{\text{rms}} = 0.67$.

In all previous tests, we fit our projections to the analytic surface brightness model, so numerical projection errors limited how far we could reduce the noise. For our final test we “removed” these errors by using the numerical projection of the density model as the image, so that as the model observational noise approaches zero there is a numerical solution with $\chi^2/N_{\text{data}} = 0$. Figure 4 shows a sequence of deprojections of the same $q_0 = 0.6$ model, with $i = 30^\circ$, in which the solution was biased to $q_b = 0.3$ and $q_b = 0.9$, and the stated error level was gradually decreased from $\sigma_0 = 0.01$ to $\sigma_0 = 10^{-4}$ (no artificial noise was added); for speed, a coarser density grid was used ($N_r \times N_a = 52 \times 13$). The allowed ellipticity range in the density decreased as σ_0 decreased, but at a much slower rate than the residuals in the image (Figure 5). For a true konus solution we should see the rms variation of the density become constant and finite at zero noise, but the presence of any noise always allows the variations to be larger. Gerhard & Binney (1996) refer to such additional degeneracies as “truncated konus densities”, whose projections are never exactly zero but have large rms density variations for very small projected surface densities. The continued presence of a coherent 46% rms density variation, even in the limit that the errors are one hundred times smaller than typical observational data, means that for all practical purposes we have found true degeneracies of the projection operator rather than any numerical effect.

3.4. Dynamical Consequences

The existence of a deprojection degeneracy is only of academic importance unless it has dynamical consequences. The fundamental question is whether the dynamical uncertainties introduced by the deprojection uncertainties can alter the conclusions of constant mass-to-light ratio, axisymmetric, two-integral dynamical models (e.g. van der Marel 1991). For a fixed mass-to-light ratio, we calculated the velocities (as described in §2.3) in the meridional plane, σ^2 and $\langle v_\phi^2 \rangle$, and the projected mean square line-of-sight velocity $\langle v_{\text{los}}^2 \rangle$ for solutions to the analytic galaxy image ($q_0 = 0.6$); these velocity profiles are shown in Figure 6 as a function of inclination and bias function. The total luminosity (and thus the total mass) of the solutions is fixed, and the average radial distribution of the luminosity cannot vary a great deal, so the total meridional plane velocities $\sqrt{2\sigma^2 + \langle v_\phi^2 \rangle}$ (and thus the kinetic energy) remain essentially constant, with variations typically $\lesssim 20\%$ at 30° and

$\lesssim 3\%$ at 90° ; this is a consequence of the virial theorem. However, the velocity anisotropy $\langle v_\phi^2 \rangle^{1/2} / \sigma$ varies considerably, with larger variations at lower inclinations ($\lesssim 60\%$ at 30° vs. $\lesssim 25\%$ at 90°). Projection of these velocities results in weak variations in the line-of-sight velocities, taking the form of alterations in the ratio between the major and minor axis profiles. Typical variations in $\langle v_{\text{los}}^2 \rangle^{1/2}$ at $i = 90^\circ$ are $\lesssim 10\%$, at $i = 60^\circ$ are $\lesssim 20\%$, and at $i = 30^\circ$ are $\lesssim 30\%$. Such variations are roughly comparable to typical measurement errors in line-of-sight velocities.

4. REAL EXAMPLES: NGC 7619 AND NGC 1439

For our final experiment we selected for deprojection two galaxies from van der Marel (1991), NGC 7619 and NGC 1439; these galaxies were chosen for their small isophote twists. The photometric profiles were taken from Franx, Illingworth, & Heckman (1989a, hereafter FIHa), where the R-band photometry is parametrized by an “intermediate” axis ($m \equiv \sqrt{ab}$) profile for each galaxy, along with the ellipticity, isophote twist, and higher-order isophote corrections at each radial point. We converted the data into a series of radial profiles and their errors at 7 evenly spaced angles beginning on the major axis and ending on the minor axis. We incorporated the isophote twist and $\cos 4\psi$ terms into our data, but none of the other higher order terms (strictly speaking, the isophote twist, which is an indicator of triaxiality, violates our density symmetry requirements, but in practice its presence was of little consequence for the final solutions). We made no corrections for the seeing, so the density profiles inside ~ 5 arcseconds will be unreliable. The photometric uncertainties are dominated by flat-fielding errors (at the 1% level) except at the outer radii, where there is a sky level uncertainty of 1%-3%. Both galaxies were deprojected for a variety of inclinations and biasing parameters.

The kinematic data were taken from Jedrzejewski & Schechter (1989, hereafter JS) and from Franx, Illingworth, & Heckman (1989b, hereafter FIHb), where the velocity dispersion and rotation velocity are given along the major and minor axes. The line-of-sight velocities were then derived from the density solution as in §3.4, and fit to the kinematic data (by minimizing the χ^2 between them) to find the R -band mass-to-light ratio Υ_R ; to minimize the effects of seeing on the results, and to allow for direct comparison with van der Marel (1991), any velocity data point inside 4 arcsec is not used in the fit. Several of these solutions are shown in Figures 7 and 8.

NGC 7619 is an E2/E3 elliptical with a small ($< 13^\circ$) isophote twist; van der Marel (1991) was not able to fit an acceptable axisymmetric two-integral dynamical model for this galaxy. The projected ellipticity varies from 0.16 to 0.28, with small ($< 0.7\%$) higher-order corrections. As is evident from the residuals in Figure 7, there is a radial “kink” in the outer regions of the galaxy ($r \sim 50$ arcsec) which cannot be well fit by a single power-law. The deprojections can be made modestly more or less elliptical, with some solutions showing boxy and “S0-like” structures. The range of the solutions is not as large as found for the test galaxies (compare Figure 7 to Figure 3), probably because much of the “smoothness” was taken up in trying to fit to a single radial power-law. The rms fractional density variations between the extreme solutions ($q_b = 0.9$ and $q_b = 0.5$)

for inclinations of 90° , 60° , and 40° are $\langle(\nu_{0.5} - \nu_{0.9})/\nu_{0.9}\rangle_{\text{rms}} = 0.07$, 0.15 , and 0.34 , respectively ($i = 40^\circ$ was used because a convergence difficulty caused minimization time to be prohibitive for $i = 30^\circ$). For $i = 90^\circ$, the solutions (with different biases q_b) had R -band mass-to-light ratios of $(\Upsilon/\Upsilon_\odot)_R \simeq (3.9 \pm 0.2)h_{50}$ and $\chi^2/N \sim 2.8$ for the kinematic fit, where $H_0 = 50h_{50} \text{ km s}^{-1} \text{ Mpc}^{-1}$; the error bars represent the range of solutions with $\Delta\chi^2 = \pm 4$ (where the poor fits of these solutions were renormalized to set $\chi^2 = N$). For $i = 60^\circ$, the range of solutions had $(\Upsilon/\Upsilon_\odot)_R \simeq (3.8-3.9 \pm 0.3)h_{50}$ and $\chi^2/N \sim 3.2-4.3$. For $i = 40^\circ$, the solutions had $(\Upsilon/\Upsilon_\odot)_R \simeq (4.1 \pm 0.3)-(4.1 \pm 0.4)h_{50}$ and $\chi^2/N \sim 3.4-5.8$. Given the uncertainties and the fact that neither we nor van der Marel found an acceptable ($\chi^2/N \sim 1$) solution for the velocities, our mass-to-light ratios Υ_R are consistent with van der Marel's $(\Upsilon/\Upsilon_\odot)_R \simeq (4.0 \pm 0.1)h_{50}$ at 90° and $(\Upsilon/\Upsilon_\odot)_R \simeq (4.1 \pm 0.1)h_{50}$ at 60° .

The second galaxy, NGC 1439, is an E1 elliptical with a small twist angle $< 9^\circ$ and an indication of a disklike distortion in the inner parts (FIHa). The projected ellipticity varies from 0.07 to 0.11, with higher-order corrections $< 0.8\%$. It has a counter-rotating core (FIHb). As can be seen in the residuals in Figure 8, the projected galaxy has a strong variation in ellipticity with radius which is not well fit by a constant ellipticity. Solutions biased toward high ellipticities again develop disk-like structures that sometimes show a feature along a line at the inclination angle from the symmetry axis. The rms fractional density variations between the extreme solutions ($q_b = 1.0$, $q_b = 0.6$) for inclinations of 90° , 60° , and 30° are $\langle(\nu_{0.6} - \nu_{1.0})/\nu_{1.0}\rangle_{\text{rms}} = 0.05$, 0.11 , and 0.33 , respectively. For $i = 90^\circ$, the solutions had $(\Upsilon/\Upsilon_\odot)_R \simeq (2.3 \pm 0.3)h_{50}$ and $\chi^2/N \sim 1.7$. For $i = 60^\circ$, the solutions had $(\Upsilon/\Upsilon_\odot)_R \simeq (2.3 \pm 0.3)h_{50}$ and $\chi^2/N \sim 1.7-1.8$. For $i = 30^\circ$, the solutions had $(\Upsilon/\Upsilon_\odot)_R \simeq (2.4-2.5 \pm 0.3)h_{50}$ and $\chi^2/N \sim 1.6-1.8$. Given the uncertainties, our mass-to-light ratios are consistent with van der Marel's $(\Upsilon/\Upsilon_\odot)_R \simeq (2.2 \pm 0.1)h_{50}$.

Both galaxies show similar variations of the line-of-sight velocities. The velocities in the meridional plane show large variations ($\lesssim 20\%$ for NGC 1439 at $i = 30^\circ$), creating differences in the projected velocities that are smaller ($\lesssim 7\%$) than typical measurement errors. The same geometric effects which create the konus densities appear to also create “konus velocities” whose large amplitudes in the meridional plane practically vanish in projection; thus, considerable refinement of spectroscopic techniques would be needed to rule out any deprojection degeneracies with velocity measurements. It is possible that higher-order velocity moments are not as strongly affected by the konus degeneracy, but an analysis of this question was outside the scope of this paper. Note that none of the solutions actually fits the velocity data well. While this does not alter our conclusions about the degeneracy of a real deprojection solution, an accurate model would need to account for seeing effects, a varying mass-to-light ratio, anisotropies, and triaxiality, in order to acceptably fit the data. Note also that only two-integral models were used, and it is possible that three-integral axisymmetric models would show larger kinematic variation in projection.

5. CONCLUSIONS

The deprojection of an axisymmetric galaxy is uniquely specified only if $i = 90^\circ$ and the symmetry axis is in the plane of the sky. At all other inclinations there is a gradually increasing degeneracy in the projection operator corresponding to an unconstrained “cone of ignorance” with opening angle $90^\circ - i$ in the Fourier transform of the density (Rybicki 1987). Recent analytic studies by Gerhard & Binney (1995) and Kochanek & Rybicki (1996) have found simple density functions, called konus densities, that are invisible in projection because their Fourier transforms are non-zero only in the cone of ignorance.

We have developed a new deprojection method based on linear regularization and explored the effects of the deprojection degeneracy on the inferred structure and dynamics of axisymmetric elliptical galaxies. The advantages of our approach over earlier methods are that it is non-parametric, that it performs a well-defined statistical fit to the surface brightness data, that it strictly enforces the positivity and monotonicity of the solution, and that it allows us to explore the degeneracies of the projection operator. The standard method of Lucy (1974) is non-parametric but does not have a well-defined convergence criterion, and functional fitting methods such as Palmer’s (1994) and Bendinelli’s (1991) depend on parametric forms. No previous method has been able to explore the degeneracies of the projection operator, or to impose monotonicity or any analytic requirement on the models.

We find that axisymmetric galaxies have large deprojection uncertainties at modest inclinations even when we are restricted to positive definite, monotonic density distributions. The uncertainties are not due to numerical projection errors, insufficient grid resolution, or observational noise, although increasing the noise in the observations increases the uncertainty. Even when the observational error in the surface brightness points approaches 10^{-4} mag, it is possible to have density distributions fitting the data with rms fractional variations of 46% for $i = 30^\circ$. The differences between the model densities are the konus densities, and they resemble the analytic solutions found by Gerhard & Binney (1995) and Kochanek & Rybicki (1996). If the bias function used to produce variations in the model density is not too spherical or too elliptical compared to the true density, the resulting model density looks reasonable. Solutions biased toward very high ellipticities show strong “disk-like” structures with a feature at angle i from the equatorial plane, and could be rejected as physical inversions. Because of the noise and konus degeneracy, the solutions are quite sensitive to the choice of the bias function; we chose simple functions which do not reproduce well some of the more complicated features in the data (e.g. NGC 7619’s radial kink), but one could easily implement a more “accurate” bias by using Lucy’s method or a parameterized approximate deprojection method to arrive at an initial bias function.

We have evaluated the dynamical variations allowed by the deprojection uncertainties in the constant mass-to-light ratio, axisymmetric, two-integral dynamical model (Binney et al. 1990; van der Marel 1991). Although the velocities in the meridional plane can have large variations, the variations in the projected mean square velocities are modest for all inclinations when compared

to typical measurement errors. Given our structural and dynamical assumptions, current velocity measurements are not helpful in reducing the deprojection degeneracy — the konus densities are associated with what we might term “konus velocities”. We infer mass-to-light ratios for NGC 1439 and NGC 7619 which are comparable to those of van der Marel (1991), but with larger uncertainties. None of the constant mass-to-light models fits the data well, with typical $\chi^2/N_{\text{dof}} \simeq 1.5\text{-}3$.

The implications of our results for more complicated models are unclear. Statler (1994a, 1994b) and Statler & Fry (1994) have used dynamical models to tightly constrain the deprojection of a triaxial galaxy, but they have assumed axis-ratios constant with radius, severely limiting the generality of the solution. Merritt (1996) has developed a technique for deriving a unique two-integral distribution function from surface brightness and velocity moment measurements, but only at the non-degenerate edge-on inclination; presumably, the large uncertainty in the density due to the degeneracy must also affect the inferred distribution function.

ACKNOWLEDGMENTS

We thank George Rybicki, Dan Fabricant, and Roeland van der Marel for their helpful comments.

REFERENCES

Arnold, R., Robijn, F. H. A., & de Zeeuw, P. T. 1995, in Fresh Views of Elliptical Galaxies, ed. A. Buzzoni, A. Renzini, & A. Serrano (San Francisco: ASP), 23

Bendinelli, O. 1991, *ApJ*, 366, 599

Bertola, F., Bettoni, D., Danziger, J., Sadler, E., Sparke, L., & de Zeeuw, T. 1991, *ApJ*, 373, 369

Binney, J. J., Davies, R. L., & Illingworth, G. D. 1990, *ApJ*, 361, 78

Binney, J., & Tremaine, S. 1987, Galactic Dynamics (Princeton: Princeton Univ. Press)

Carollo, C. M., & Danziger, I. J. 1994, *MNRAS*, 270, 743

Carollo, C. M., de Zeeuw, P. T., van der Marel, R. P., Danziger, I. J., & Qian, E. E. 1995, *ApJ*, 441, L25

Dehnen, W. 1995, *MNRAS*, 274, 919

Dehnen, W., & Gerhard, O. E. 1993, *MNRAS*, 261, 311

Dehnen, W., & Gerhard, O. E. 1994, *MNRAS*, 268, 1019

Fabbiano, G. 1989, *ARA&A*, 27, 87

Fabbiano, G. 1995, in Fresh Views of Elliptical Galaxies, ed. A. Buzzoni, A. Renzini, & A. Serrano (San Francisco: ASP), 103

Franx, M., Illingworth, G., & de Zeeuw, T. 1991, *ApJ*, 383, 112

Franx, M., Illingworth, G., & Heckman, T. 1989a, *AJ*, 98, 538 (FIHa)

Franx, M., Illingworth, G., & Heckman, T. 1989b, *ApJ*, 344, 613 (FIHb)

Franx, M., van Gorkom, J. H., & de Zeeuw, T. 1994, *ApJ*, 436, 642

Gerhard, O. 1991, *MNRAS*, 250, 812

Gerhard, O., & Binney, J. 1996, *MNRAS*, in press

Hunter, C., & Qian, E. 1993, *MNRAS*, 262, 401

Jedrzejewski, R. & Schechter, P. L. 1989, *AJ*, 98, 147

Kochanek, C. S. 1995, *ApJ*, 445, 554

Kochanek, C. S. 1996, *ApJ*, in press

Kochanek, C. S., & Rybicki, G. B. 1996, *MNRAS*, in press

Lucy, B. 1974, *AJ*, 79, 745

Merritt, D. 1996, *AJ*, in press

Maoz, D., & Rix, H.-W. 1993, *ApJ*, 416, 425

Newton, A. J., & Binney, J. 1984, *MNRAS*, 210, 711

Palmer, P. L. 1994, *MNRAS*, 266, 697

Press, W. H., Teukolsky, S. A., Vetterling, W. T., & Flannery, B. P. 1992, Numerical Recipes in C, 2nd Ed. (Cambridge: Cambridge Univ. Press)

Qian, E. E., de Zeeuw, P. T., van der Marel, R. P., & Hunter, C. 1995, MNRAS, 274, 602

Rix, H.-W., & White, S. D. M. 1990, ApJ, 362, 52

Rybicki, G. B. 1987, in Structure and Dynamics of Elliptical Galaxies, ed. P. T. de Zeeuw (Dordrecht: Kluwer), 397

Saglia, R. P., et al. 1993, ApJ, 403, 567

Satoh, C. 1980, PASJ, 32, 41

Schweizer, F., Whitmore, B. C., & Rubin, V. C. 1983, AJ, 88, 909

Statler, T. S. 1994a, ApJ, 425, 458

Statler, T. S. 1994b, ApJ, 425, 500

Statler, T. S. 1995, in Fresh Views of Elliptical Galaxies, ed. A. Buzzoni, A. Renzini, & A. Serrano (San Francisco: ASP), 27

Statler, T. S., & Fry, A. N. 1994, ApJ, 425, 481

van der Marel, R. P., Binney, J., & Davies, R. L. 1990, MNRAS, 245, 582

van der Marel, R. P. 1991, MNRAS, 253, 710

van der Marel, R. P., Evans, N. W., Rix, H.-W., White, S. D. M., & de Zeeuw, T. 1994, MNRAS, 271, 99

Whitmore, B. C., McElroy, D. B., & Schweizer, F. 1987, ApJ, 314, 439

APPENDICES

A. First-Order Projection Scheme

From the interpolated density of equation (6), we find its contribution to the projection:

$$\begin{aligned} dI_{jklm} &= \int_{z_1}^{z_2} \left(\check{\nu}_{jk} + \frac{\check{\nu}_{jk+1} - \check{\nu}_{jk}}{r_k - r_{k+1}} r_k \right) dz - \int_{z_1}^{z_2} \frac{\check{\nu}_{jk+1} - \check{\nu}_{jk}}{r_k - r_{k+1}} r(z) dz \\ &= \left(\check{\nu}_{jk} + \frac{\check{\nu}_{jk+1} - \check{\nu}_{jk}}{r_k - r_{k+1}} r_k \right) (z_2 - z_1) - \frac{\check{\nu}_{jk+1} - \check{\nu}_{jk}}{r_k - r_{k+1}} \int_{z_1}^{z_2} r(z) dz. \end{aligned} \quad (\text{A1})$$

Since $r^2 = \varpi^2 + z^2$,

$$\begin{aligned} \int r dz &= \int_{z_1}^{z_2} (\varpi^2 + z^2)^{1/2} dz \\ &= \frac{z}{2} \sqrt{\varpi^2 + z^2} + \frac{\varpi^2}{2} \ln \left(z + \sqrt{\varpi^2 + z^2} \right) \\ &= \frac{zr}{2} + \frac{\varpi^2}{2} \ln(z + r), \end{aligned} \quad (\text{A2})$$

which leads to the first-order approximation in equation (7).

B. Gradient Expressions

The derivatives of the χ^2 statistic are:

$$\chi_{in}^2' \equiv \frac{\partial \chi^2}{\partial p_{in}} = 2p_{in} \sum_{lm} \frac{I_{lm} - I_{lm}^*}{\sigma_{lm}^2} A_{inlm}, \quad (\text{B1})$$

$$\chi_{in}^2'' = \frac{\chi_{in}^2'}{p_{in}} + 2\check{\nu}_{in} \sum_{lm} \left(\frac{A_{inlm}}{\sigma_{lm}} \right)^2, \quad (\text{B2})$$

where

$$\begin{aligned} A_{inlm} \equiv & \Delta z_{i-1lm} - \Delta z_{inlm} \\ & + 2 \cdot \left(\frac{\Delta z_{inlm} r_{n+1}}{r_{n+1} - r_n} + \frac{\Delta z_{in-1lm} r_{n-1}}{r_{n-1} - r_n} \right) \\ & + \frac{1}{r_n - r_{n+1}} \left[z_2 r_2 - z_1 r_1 + \varpi_{lm}^2 \ln \left(\frac{z_2 + r_2}{z_1 + r_1} \right) \right]_{inlm} \\ & + \frac{1}{r_n - r_{n-1}} \left[z_2 r_2 - z_1 r_1 + \varpi_{lm}^2 \ln \left(\frac{z_2 + r_2}{z_1 + r_1} \right) \right]_{in-1lm}. \end{aligned} \quad (\text{B3})$$

The derivatives of the radial and angular smoothness parameters H_1 and H_2 are:

$$(H_1)'_{in} = 4p_{in} \sum_{j=i}^{N_a-1} \begin{cases} \frac{h_{jn}}{h_{jn-1}\nu_{jn-1}} \left(\frac{h_{jn}\nu_{jn}}{h_{jn-1}\nu_{jn-1}} - 1 \right), & n > 0 \\ \frac{h_{jn+1}\nu_{jn+1}}{h_{jn}\nu_{jn}^2} \left(1 - \frac{h_{jn+1}\nu_{jn+1}}{h_{jn}\nu_{jn}} \right), & n < N_r - 1 \end{cases} \quad (B4)$$

$$(H_1)''_{in} = \frac{(H_2)'_{in}}{p_{in}} + 8\tilde{\nu}_{in} \sum_{j=i}^{N_a-1} \begin{cases} \frac{h_{jn}^2}{h_{jn-1}\nu_{jn-1}^2}, & n > 0 \\ \frac{h_{jn+1}\nu_{jn+1}}{h_{jn}\nu_{jn}^3} \left(\frac{3h_{jn+1}\nu_{jn+1}}{h_{jn}\nu_{jn}} - 2 \right), & n < N_r - 1 \end{cases} \quad (B5)$$

$$(H_2)'_{in} = 4p_{in} \times \begin{cases} \frac{h_{in}}{h_{i-1n}\nu_{i-1n}} \left(\frac{h_{in}\nu_{in}}{h_{i-1n}\nu_{i-1n}} - 1 \right), & i > 0 \\ \sum_{j=l}^{N_a-2} \frac{h_{j+1n}\tilde{\nu}_{j+1n}}{h_{jn}\nu_{jn}^2} \left(1 - \frac{h_{j+1n}\nu_{j+1n}}{h_{jn}\nu_{jn}} \right), & i < N_a - 1 \end{cases} \quad (B6)$$

$$(H_2)''_{in} = \frac{(H_2)'_{in}}{p_{in}} + 8\tilde{\nu}_{in} \times \begin{cases} \left(\frac{h_{in}}{h_{i-1n}\nu_{i-1n}} \right)^2, & i > 0 \\ \sum_{j=l}^{N_a-2} \frac{h_{j+1n}\tilde{\nu}_{j+1n}}{h_{jn}\nu_{jn}^3} \left[\frac{h_{j+1n}}{h_{jn}} \left(\frac{3\tilde{\nu}_{j+1n}}{\nu_{jn}} + 2 \right) - 2 \right], & i < N_a - 1 \end{cases} \quad (B7)$$

CAPTIONS

Fig. 1.— Effects of the bias function on deprojections of an artificial galaxy image. Each column represents a different choice for the bias function. The top row shows the normalized residuals of the solution, $(I - I^*)/\sigma$, where the horizontal dotted lines are the one-standard-deviation errors. The dashed lines are the residuals of the projection of the “correct” density (i.e. they show the added “noise”), and the curves are offset for visibility with the major axis on top. The second row shows the deprojected density profiles on fixed azimuths. The third row shows contour plots of the density solution (solid contours) and the “correct” density (dotted contours). There are 26 contour levels shown, logarithmically spaced from $\nu = 0.25$ to $\nu = 2.5 \times 10^{-6}$. The bottom row shows contour plots of the konus density, or the difference between the final solution and the “correct” density; dotted contours represent negative values. There are 42 contour levels shown (positive and negative), logarithmically spaced from $\nu = 10^{-2}$ to $\nu = 10^{-6}$.

Fig. 2.— The effects of numerical resolution on deprojections of artificial galaxy images. The inclination is fixed at $i = 30^\circ$. The major-to-minor axis ratio is plotted for each solution as a function of radius. The “correct” solution is the central dashed line with $q_0 = 0.6$; the upper and lower sets of curves are the solutions when biased toward $q_b = 0.9$ and $q_b = 0.3$. The solid, dashed, dotted, and dot-dashed curves show the solutions when the density zone resolution is $N_r \times N_a = 100 \times 25$, 80×20 , 40×10 , 28×7 , and 20×5 , respectively. Note that the image resolution is $N_x \times N_y = 46 \times 7$, so the density is overconstrained by the data in the last two cases.

Fig. 3.— Deprojections of an artificial galaxy image as a function of noise level and inclination. Each column represents a different assumed inclination i , with $i = 90^\circ$, 60° , and 30° , from left to right. In the two top rows, the solid, dotted, and dot-dashed lines show solutions with decreasing fractional noise σ_0 . The highest noise level is set to a realistic value; the lowest is the level at which numerical errors become significant. The top row shows the density axis ratio, where the central dashed line is the deprojection using the “correct” bias. The middle row shows the density solution angular profile at a fixed radius ($r/s_0 = 1.6$). The bottom row shows contours of the solution density. The dotted and dashed lines show solutions at the highest (normal) noise level ($q_b = 0.9$ and $q_b = 0.3$, respectively); the solid contours show the “correct” solution, $q_0 = 0.6$. There are 26 contour levels shown, logarithmically spaced from $\nu = 0.25$ to $\nu = 2.5 \times 10^{-6}$.

Fig. 4.— Deprojection of an artificial galaxy image with numerical errors removed (see text), as a function of the noise level σ_0 . The inclination is fixed at $i = 30^\circ$. The axis ratio is plotted for each solution. The “correct” solution is the central dotted line with $q_0 = 0.6$; the upper and lower sets of curves are the solutions when biased toward $q_b = 0.9$ and $q_b = 0.3$. The solid curves show a sequence of solutions with noise level σ_0 lowered.

Fig. 5.— Effects of observational errors on deprojection. The rms fractional variation in the density solution and the rms fractional error in its projected image are shown as a function of error level. The dotted line solutions were biased toward $q_b = 0.3$, and the solid line solutions were biased

toward $q_b = 0.9$.

Fig. 6.— Velocity dispersions for an analytic test galaxy ($q_0 = 0.6$), assuming a constant mass-to-light ratio. The left column shows the velocities in the meridional plane, along the major axis (the variations along the minor axis were inconsequential). The right column shows the projected velocities along the major (upper profiles) and minor (lower profiles) axes. The top box shows solutions for $i = 90^\circ$, the middle for 60° , and the bottom for 30° . At each inclination, solutions are shown with biases of $q_b = 0.9, 0.6$, and 0.3 . The vertical axis has arbitrary units.

Fig. 7.— Deprojection solutions and resultant projected velocities for NGC 7619, for varying inclination and bias function. Each column represents a different assumed inclination i . The top row shows the normalized residuals of the solution: $(I - I^*)/\sigma$, where the horizontal dotted lines are the one-standard-deviation errors. The middle row shows the rms line-of-sight velocity profile for the major (upper) and minor (lower) axes. Velocity data (JS; FIHb) are superimposed, where the crosses are major axis points, the solid squares are minor axis points, and the error-bars are one- σ errors. The bottom row shows contours of the solution density. There are 28 contour levels, from $\nu = 0.25$ to $\nu = 10^{-6}$. The solid lines indicate a solution with a $q_b = 0.7$ bias function; the dotted lines, $q_b = 0.9$; the dashed lines, $q_b = 0.5$. The vertical dot-dash line indicates the cut-off radius (4 arc sec) below which the velocity data are not used.

Fig. 8.— Deprojection solutions and resultant projected velocities for NGC 1439, for varying inclination and bias function. Velocity data are from FIHb. Labels are the same as in Fig. 7. There are 24 contour levels, from $\nu = 0.25$ to $\nu = 6.3 \times 10^{-6}$. The solid lines indicate a solution with a $q_b = 0.8$ bias function; the dotted lines, $q_b = 0.99$; the dashed lines, $q_b = 0.6$.

This figure "fig1.gif" is available in "gif" format from:

<http://arxiv.org/ps/astro-ph/9609202v1>

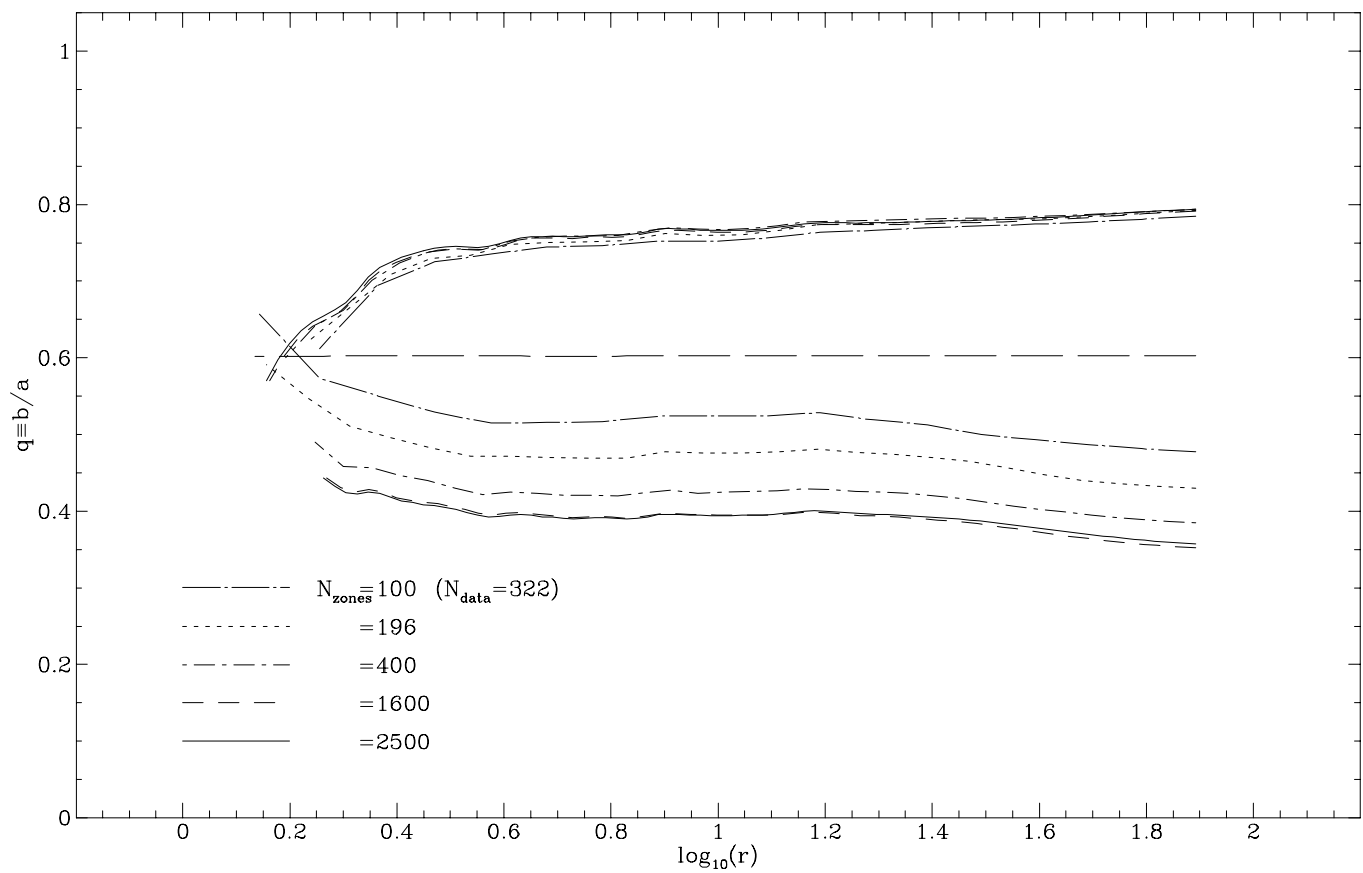


Figure 2

This figure "fig3.gif" is available in "gif" format from:

<http://arxiv.org/ps/astro-ph/9609202v1>

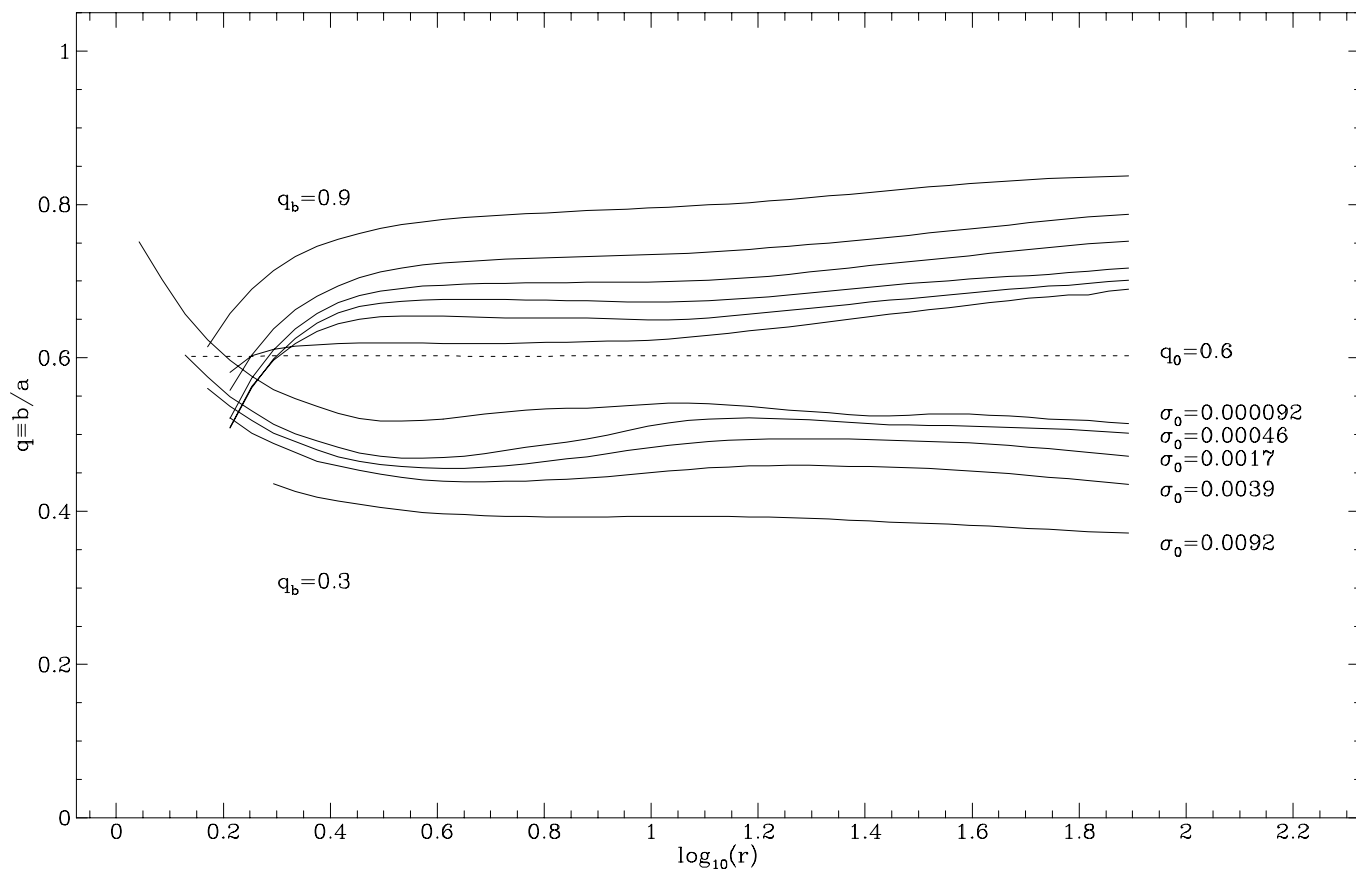


Figure 4

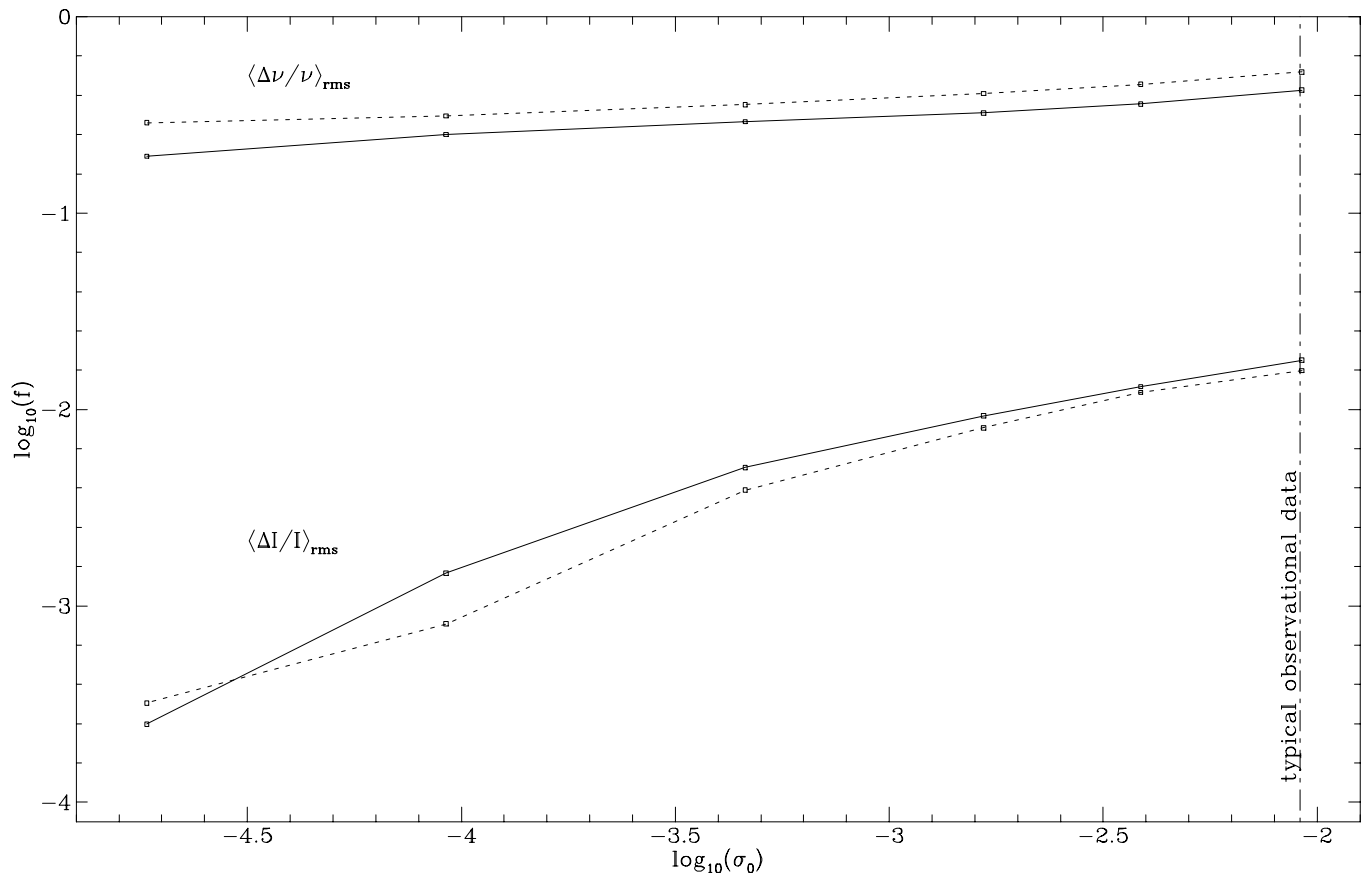


Figure 5

This figure "fig6.gif" is available in "gif" format from:

<http://arxiv.org/ps/astro-ph/9609202v1>

This figure "fig7.gif" is available in "gif" format from:

<http://arxiv.org/ps/astro-ph/9609202v1>

This figure "fig8.gif" is available in "gif" format from:

<http://arxiv.org/ps/astro-ph/9609202v1>